PHYSICAL REVIEW C **93**, 034603 (2016)

Fragment-mass, kinetic energy, and angular distributions for ^{234}U(n,f) at incident neutron energies from $E_n = 0.2$ MeV to 5.0 MeV

A. Al-Adili,[1,2] F.-J. Hambsch,[1,*] S. Pomp,[2] S. Oberstedt,[1] and M. Vidali[1]
[1]*European Commission, Joint Research Centre, Institute for Reference Materials and Measurement (IRMM), B-2440 Geel, Belgium*
[2]*Department of Physics and Astronomy, Uppsala University, Box 516, 751 20 Uppsala, Sweden*

(Received 19 August 2015; published 3 March 2016)

This work investigates the neutron-induced fission of ^{234}U and the fission-fragment properties for neutron energies between $E_{\rm n} = 0.2$ and 5.0 MeV with a special highlight on the prominent vibrational resonance at $E_{\rm n} = 0.77$ MeV. Angular, energy, and mass distributions were determined based on the double-energy technique by means of a twin Frisch-grid ionization chamber. The experimental data are parametrized in terms of fission modes based on the multimodal random neck-rupture model. The main results are a verified strong angular anisotropy and fluctuations in the energy release as a function of incident-neutron energy.

DOI: 10.1103/PhysRevC.93.034603

I. INTRODUCTION

The fission properties of the uranium isotopes have been investigated throughout the 75 years since the discovery of fission. Due to the importance to the nuclear-energy industry, the fissioning systems ^{236}U* and ^{239}U* have been the main targets. The third uranium isotope naturally abundant in very small fractions is ^{234}U. Accurate data are needed on ^{234}U(n,f), e.g., for the modeling of the ^{236}U* reaction, at the excitation energies where second-chance fission is possible. However, this isotope has received much less attention, which resulted in a lack of ^{234}U(n,f) fission-fragment data in the nuclear-data libraries. For instance, no mass-yield distributions are available for this reaction. In addition, nuclear data on ^{234}U are relevant for nuclear-waste management and for the Th-U cycle.

Considering basic fission research, a few studies have revealed interesting fluctuations in the fission-fragment properties for this reaction. Significant changes were observed in the angular and energy distributions around the vibrational resonance at $E_{\rm n} = 0.77$ MeV [1–4]. Further accurate data are needed to increase the knowledge about the physics of vibrational resonances, especially by studying the mass and energy distributions. The large fluctuation in angular anisotropy could have an impact on the mass distribution, a correlation which has not yet been fully explored (see Ref. [5], p. 494). The present work continues the investigation campaign of the uranium isotopes carried out by the JRC-IRMM [6–9]. The ^{234}U(n,f) reaction was studied in terms of angular, mass, and energy distributions, at 14 different incident-neutron energies, $E_{\rm n}$, ranging from 0.2 to 5.0 MeV.

II. EXPERIMENTS

The measurements were performed at the monoenergetic Van de Graaff accelerator of the JRC-IRMM in Geel, Belgium. Three different reactions were used to produce the incident neutrons at different energies, tabulated in Table I. The ^{234}UF$_4$ sample (92.13 ±0.46 μgU/cm^2) used for neutron irradiation was produced through vacuum evaporation on a polyimide backing (32.0 ± 1.5 μg/cm^2) covered with Au (50 μg/cm^2). The fragments were detected by means of a twin Frisch-grid ionization chamber (TFGIC) which operated with P-10 gas (90% Ar + 10% CH$_4$), at a gas pressure of 1.05×10^5 Pa and a gas flow of 0.1 ℓ/min. The chamber, shown in Fig. 1, consists of five electrodes: two anodes (A), two Frisch grids (G), and one common cathode (C). The two fragments enter the counting gas and ionize the atoms, creating free electron-ion pairs. The electrons drift toward the anode plates, due to the potential difference, and thus induce charge signals on the five chamber electrodes. These signals were fed into charge-sensitive preamplifiers. Both conventional analog and modern digital data-acquisition systems were used in parallel to optimize the setup and search for possible improvements. In the digital case, the chamber signals were digitized by 100-MHz waveform digitizers and stored for offline analysis. The comparison between the analog and digital signals revealed a superior digital performance with a successful α pile-up correction, better drift stability, and a better angular resolution as discussed in Refs. [10,11]. On this basis the digital data were chosen for further analysis. The absolute energy calibration was done by measuring ^{235}U$(n_{\rm th},f)$ [6,12]. The values of total kinetic energy, $\overline{\rm TKE} = 170.5 \pm 0.5$ MeV, and mean heavy mass, $\langle A_{\rm H}\rangle = 139.6 \pm 0.1$ u, were taken from Ref. [5] (p. 323) to be used for the calibration. The ^{235}UF$_4$ sample (45 ± 2 μgU/cm^2) was also produced by vacuum evaporation on a polyimide backing covered by Au (53 ± 0.6 μg/cm^2). In total for ^{234}U(n,f) 14 different neutron energies were measured, with special focus on the vibrational resonance around $E_{\rm n} = 0.77$ MeV. A summary of the full experimental series is given in Table I.

III. DATA ANALYSIS

The concept of the double-energy (2E) technique is to use the conservation of linear momentum and mass to calculate the pre-neutron-emission fragment masses. Neglecting the recoil in the neutron emission from the fission fragments (FFs), the

---

[*] Corresponding author: Franz-Josef.Hambsch@ec.europa.eu

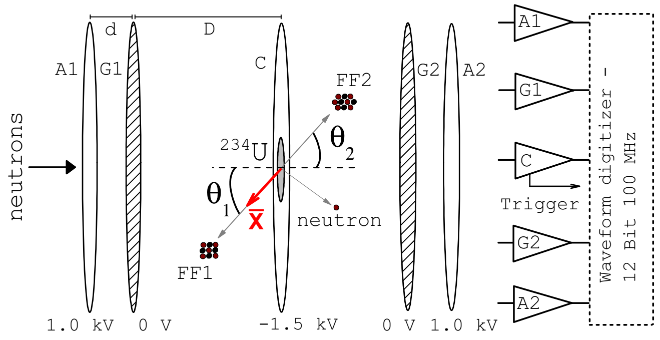

FIG. 1. The experimental setup. Neutrons induce fission in the ^{234}U target located at the center of the ionization chamber (TFGIC). Five electrodes are used: two anodes (A), two Frisch grids (G), and one common cathode (C). The signals from the charge-sensitive preamplifiers were digitized. $\overline{X}$ denotes the the center of gravity of the electron cloud ($d = 6$ mm and $D = 31$ mm).

collinearity of both FFs is nearly preserved due to the very thin samples. If the energy and emission angle for each fragment can be deduced, one can estimate the neutron emission and determine the FF mass. The energy of the FF is proportional to the induced charge on the anode plates, whereas the emission angle can be extracted from the induced charge on the grid signal.

A. Signal treatment

The total signal generated on the anode plate is

$$Q_A = -n_0 e + \sigma n_0 e \frac{\overline{X}}{D} \cos\theta, \tag{1}$$

where n_0 is the number of ion-electron pairs created from the ionization process and $\overline{X}$ is the center of gravity of the electron-cloud distribution, and D is the cathode-grid distance. The charge induced on the grid plate is

$$Q_G = n_0 e(1-\sigma)\frac{\overline{X}}{D}\cos\theta. \tag{2}$$

Both signals of Eqs. (1) and (2) are dependent on the grid inefficiency factor σ, due to the limitation of the grid in shielding the charge. The proper method for correcting this effect was recently settled in Refs. [13,14]. After the grid-inefficiency correction, the signals were corrected for baseline fluctuations and ballistic deficit (for a preamplifier decay constant of $\Gamma = 118\ \mu$s). In addition, the ^{234}U sample had a high α activity of $1.5 \times 10^5\ \alpha$/s, which added up to the detected signal amplitude. By filtering the α contribution, a successful pile-up correction was applied to the data. The α pile-up correction allowed for rejecting the α contribution without discarding the FF contribution to the signal. It is estimated that more than 90% of the α pile-ups were removed [10]. Finally, to deduce the anode signal's amplitude a CR-RC^4 filter was applied based on a Butterworth-filter design [15]. The shaping time chosen for the filter was $\tau = 1.2\ \mu$s. The aim of using a CR-RC^4 filter was to increase the signal-to-noise ratio. The output from the filter is a semi-Gaussian distribution where the amplitude is proportional to the input signal height.

B. Determination of the (fission-fragment) emission angle

The emission angle of the FF relative to the ionization chamber axis is embedded in the grid signal. However, by means of analog techniques it is difficult to treat it due to the bipolar nature of the grid signal. Thus, to preserve the angle information and to provide a unipolar signal, the anode and grid signals are usually summed [16]. This approach requires a perfect calibration between the two summed channels. By application of digital-signal processing, the bipolarity is not problematic, and the angle was successfully deduced from the grid signal as presented in Ref. [11]. The grid signal

TABLE I. Neutron energies, neutron-producing targets, and target thickness along with the acquired counting statistics. Uncertainties in the neutron energies show the incident-neutron energy spread.

Neutron energy (MeV)	Target	Target thickness (μg/cm^2)	Counting statistics
0.200 ± 0.066	^{7}LiF(p,n)	830	17 000
0.350 ± 0.057	^{7}LiF(p,n)	830	20 000
0.500 ± 0.052 (± 0.039)	^{7}LiF(p,n)	830 (619)	161 000
0.640 ± 0.035	^{7}LiF(p,n)	596	444 000
0.770 ± 0.033	^{7}LiF(p,n)	596	182 000
0.835 ± 0.034	^{7}LiF(p,n)	619	92 000
0.900 ± 0.032 (± 0.033)	^{7}LiF(p,n)	596 (619)	80 000
1.000 ± 0.111	TiT(p,n)	1936	155 000
1.500 ± 0.093 (± 0.094) (± 0.103)	TiT(p,n)	1930 (1936) (2130)	406 000
2.000 ± 0.081 (± 0.082) (± 0.089)	TiT(p,n)	1930 (1936) (2130)	895 000
2.500 ± 0.067 (± 0.072)	TiT(p,n)	1930 (1936)	711 000
3.000 ± 0.065	TiT(p,n)	1936	359 000
4.000 ± 0.309	D(d,n)	1902	81 000
5.000 ± 0.177	D(d,n)	1902	141 000
^{235}U(n_{th},f)	TiT(p,n)	1930 (2130)	1 900 000

was in some cases found to give a better angular resolution compared to the widely used summing approach. It was also found to be less sensitive to drifts; hence, the grid approach was used in the present work. To obtain the FF $\cos(\theta)$ distribution from the measured grid amplitude, the $n_0e(\overline{X}/D)$ range is plotted as a function of the fragment pulse height. The range is measured at half height of the grid distribution for each anode channel number. Equation (2) is then divided by the measured $n_0e(\overline{X}/D)$ range to get the $\cos(\theta)$ distribution. To determine the quality of this angular determination, the distributions from the sample side are usually plotted versus the backing side in a two-dimensional histogram and a 45° proportionality between the two sides is achieved. The angular resolution obtained in this work was $\Delta\cos(\theta) = 0.12$ (full width at half maximum).

C. Energy-loss correction

Once the emission angle is calculated the energy distribution is transformed to the center of mass to account for the momentum transfer of the incident neutron. Thereafter, the mean anode pulse heights from both chamber sides are plotted as a function of $1/\cos(\theta)$ as demonstrated in Fig. 2(a). The data sets are fitted linearly in the $\cos^{-1}(\theta)$ region between 1.2 and 3. Larger values are excluded since the linear energy-loss trend is no longer valid due to increased energy and angular straggling. Smaller values, where $\cos(\theta) \sim 1$, are excluded due to an additional mass dependence of $\overline{X}/D$ to be corrected at a later stage. Only events with $\cos(\theta) \geqslant 0.5$ are finally chosen for the mass determination. The slopes for the two data sets differ because of the different energy losses encountered in the sample and backing sides, respectively. Due to the thicker backing, larger energy losses are seen on the backing side. The fitted lines are extrapolated to the intersection at the y axis which corresponds to zero sample thickness, i.e., an ideal energy-loss-free channel (E_0). Each fission event is corrected for energy losses to the level of E_0. At least two different approaches are usually used for treating the energy losses of the total data set at different neutron energies. In Ref. [8] a linear fit was performed for each measured energy, whereas in Ref. [9] one fit was done to a reference energy with good statistics and kept constant for all the other energies. Two drawbacks can be attributed to the former technique. The first is that the statistics affects the quality of the fit. As a result the data for some runs might be corrected to a slightly different level and one introduces an additional parameter to alter the physical observables. The second, more serious, drawback is that any possible angular-dependent energy emission that might result from the dynamics of the fission process can easily be erased mistakenly. Such an effect was reported earlier, e.g., in Ref. [17]. Therefore, the latter method was adopted in this work, keeping in mind that the same ^{234}U sample is used for all measurements. The energy losses are assumed to be only dependent on the material traveled through and independent of the relatively small changes of the TKE. After the energy-loss correction a comparison is made for each measurement between the pulse-height distributions from both chamber sides. A very good agreement reflects the good quality of all corrections as seen in Fig. 2(b).

D. Pulse-height defect

Not all interactions with the counting gas are ionizing since some electrons recombine with free ions and neutral atoms. This effect accounts for about 3.5–4.5 MeV reduction in the detected FF energy which needs to be corrected for [16]. The pulse-height defect (ΔE_{phd}) is dependent mainly on the fragment mass and energy and can be parametrized as in Ref. [18]:

$$\Delta \mathrm{E}_{\mathrm{phd}}\left(A_{\mathrm{post}}, E_{\mathrm{post}}^{\mathrm{LAB}}\right) = \frac{A_{\mathrm{post}} E_{\mathrm{post}}^{\mathrm{LAB}}}{\alpha} + \frac{A_{\mathrm{post}}}{\beta}, \tag{3}$$

where $E_{\mathrm{post}}^{\mathrm{LAB}}$ is the fragment energy in the laboratory system after emitting prompt neutrons. The parameters α and β are fine-tuned during the absolute calibration of $^{235}\mathrm{U}(n_{\mathrm{th}}, f)$. The aim is to obtain the right ΔE_{phd} magnitude expected, e.g., from Refs. [16,19], and to arrive at the values of $\overline{\mathrm{TKE}}$ and $\langle A_{\mathrm{H}} \rangle$ as given in Ref. [5] (p. 323). Note that, because the fragments already evaporate the prompt neutrons before entering the gas, the post neutron-emission masses, A_{post}, must be used. ΔE_{phd} must be recalculated for each iteration with the new determined energies and masses (see Sec. III F).

E. Neutron multiplicities

One critical step in the analysis is to estimate the neutron emission on an event-by-event basis. Since for $^{234}\mathrm{U}(n, f)$ no data on neutron multiplicity as a function of A exist, the $\bar{\nu}_{234}(A)$ parametrization is performed based on experimental data from the neighboring isotopes (taken from Ref. [20]), $^{233}\mathrm{U}(n_{\mathrm{th}}, f)$ and $^{235}\mathrm{U}(n_{\mathrm{th}}, f)$:

$$\bar{\nu}_{234}(A) = \frac{1}{2}(\bar{\nu}_{235}(A) + \bar{\nu}_{233}(A)). \tag{4}$$

Moreover, the neutron multiplicity is dependent on the TKE. Taking this into account, the amount of neutrons per fission is estimated according to Ref. [21] as

$$\nu_{234}(A,\mathrm{TKE}) = \bar{\nu}_{234}(A) + \frac{\bar{\nu}_{234}(A)}{\bar{\nu}_{234}(A) + \bar{\nu}_{234}(A_{\mathrm{CN}} - A)} \times \frac{\langle \mathrm{TKE}(A) \rangle - \mathrm{TKE}}{E_{\mathrm{sep}}}, \tag{5}$$

where A_{CN} is the compound nucleus mass and $E_{\mathrm{sep}} = 8.6$ MeV is the neutron separation energy. Equation (5) leads to a lower neutron emission when the TKE is higher. Finally, the neutron emission is also dependent on the incident-neutron energy. When E_{n} increases, it leads to a higher excitation energy of the compound nucleus, resulting in enhanced neutron emission from the fragments. A linear interpolation to the neutron data from Ref. [22] was done to allow for an estimation of the total neutron emission as a function of incident-neutron energy. The neutron multiplicity obtained from Eq. (5) was shifted for all masses to give an average value corresponding to the linear interpolation of $\bar{\nu}_{\mathrm{tot}}$. We also tested another neutron correction method, which increases $\bar{\nu}_{\mathrm{tot}}$ only for the heavy fragments. In Ref. [23] we explored in detail the impact of the choice of the correction method on the final fission fragment properties. A brief discussion of the main differences between the results of the two methods is presented in Sec. IV C.

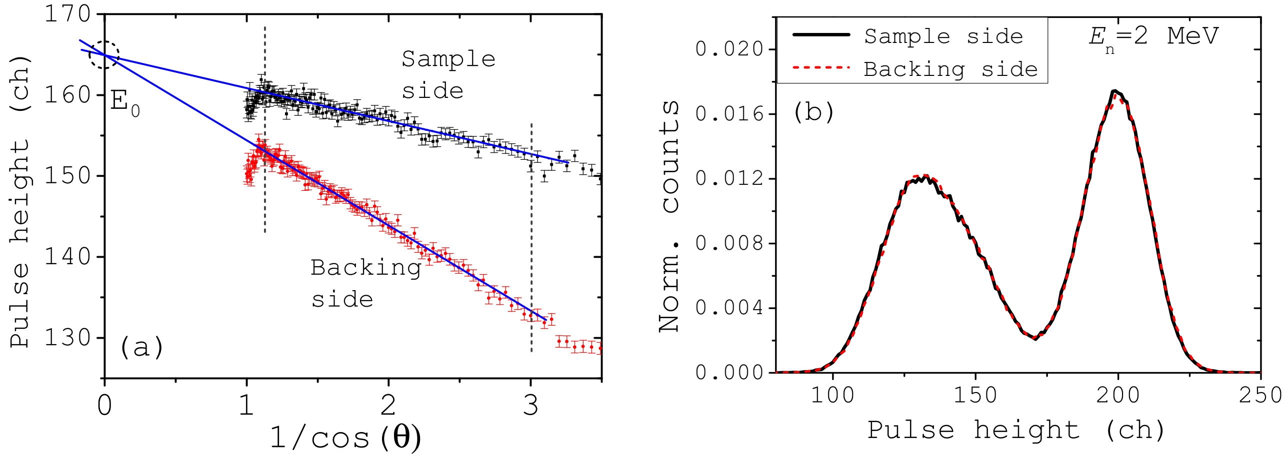

FIG. 2. (a) The energy-loss correction is done by measuring the mean pulse height as a function of $\cos^{-1}(\theta)$. The data are corrected to the E_0 level which corresponds to an ideal channel before energy losses. (b) The pulse height distributions from sample and backing sides after the energy-loss correction.

F. Mass calculations

Based on reaction kinematics we get $E_{\rm post}A_{\rm pre} \approx E_{\rm pre}A_{\rm post}$. By introducing the estimated neutron multiplicities, the pre-neutron emission energy in the laboratory system can be calculated as

$$E^{\rm lab}_{\rm pre} = \frac{A_{\rm pre}}{A_{\rm pre} - \nu(A,{\rm TKE})} E^{\rm lab}_{\rm post}, \tag{6}$$

and later transformed into the center-of-mass (c.m.) system

$$\begin{aligned} E^{\rm c.m.} &= E^{\rm lab} + A^{-2}_{\rm CN} A_{\rm n} A_{\rm pre} E^{\rm lab}_{\rm n} \\ &\pm 2A^{-1}_{\rm CN}\sqrt{A_{\rm pre}A_{\rm n}E^{\rm lab}E^{\rm lab}_{\rm n}}\cos\theta^{\rm lab}. \end{aligned} \tag{7}$$

The difference in sign is due to the incoming neutron momentum. The fragments emitted toward the backing side get a boost from the incoming neutron; hence, a subtraction is needed, and vice versa for the sample side. The final pre-neutron emission fragment masses are calculated by

$$\begin{aligned} A_{1,\rm pre} &= A_{\rm CN}E^{\rm c.m.}_{2,\rm pre}\left(E^{\rm c.m.}_{1,\rm pre} + E^{\rm c.m.}_{2,\rm pre}\right)^{-1}, \\ A_{2,\rm pre} &= A_{\rm CN}E^{\rm c.m.}_{1,\rm pre}\left(E^{\rm c.m.}_{1,\rm pre} + E^{\rm c.m.}_{2,\rm pre}\right)^{-1}. \end{aligned} \tag{8}$$

The calculations above are repeated in an iterative loop where the improved masses are always derived from masses from the earlier steps. When the mass difference, $A_{\rm new} - A_{\rm old}$, in two sequential iterations is less than $1/16$ u, the iteration is stopped.

IV. RESULTS AND DISCUSSION

In the following section we present the angular distributions, kinetic-energy distributions, and mass yields, from the 14 incident-neutron energies measured for ^{234}U(n,f). Unless stated, only statistical errors are plotted in the figures.

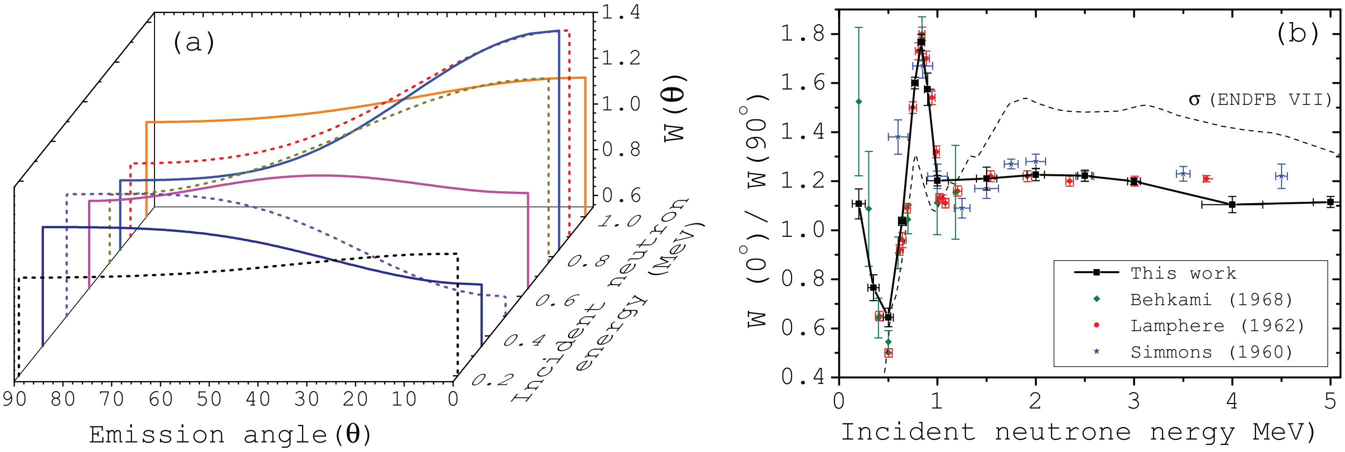

FIG. 3. (a) The full Legendre polynomial fits up to P_4, for the measurements up to $E_{\rm n} = 1.0$ MeV. (b) The angular anisotropy as a function of incident-neutron energy shows strong fluctuations around the vibrational resonances at $E_{\rm n} = 0.5$ and 0.77 MeV. Results are compared to data from Refs. [1–3], and the fission cross section (σ) is also plotted.

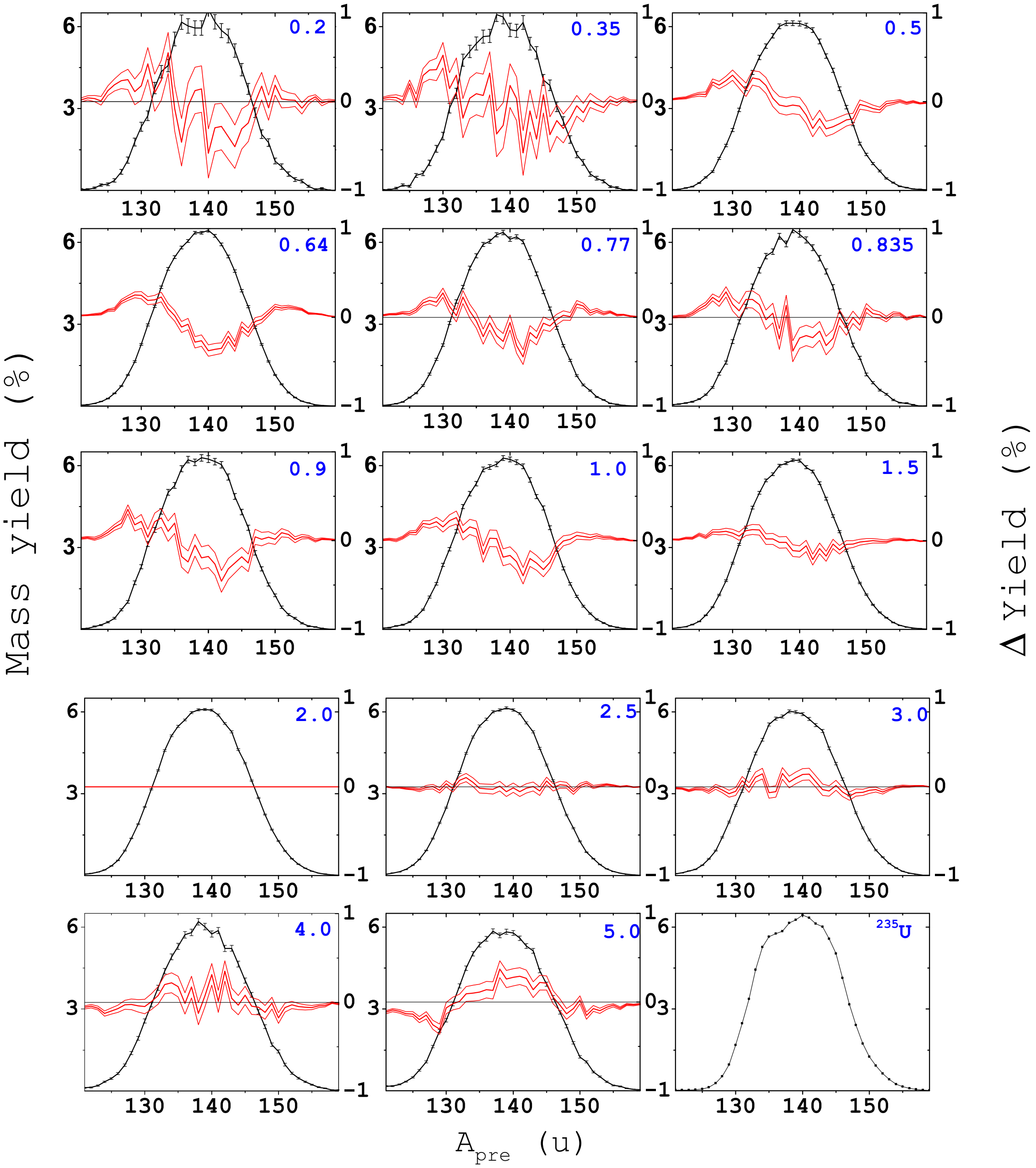

FIG. 4. The measured mass yields (black symbols, left axis) with the neutron energy listed in the upper corner. The absolute mass difference (red zigzag line, right axis) is plotted for each case, relative to $E_n = 2.0$ MeV [$\Delta Y = Y(2\text{ MeV}) - Y(E_n)$]. Statistical errors are plotted as lines.

A. Angular anisotropy

To calculate the angular anisotropy, a final correction had to be done, namely the $\overline{X}/D$ dependence on fragment mass. This is done by measuring the range (similarly to the energy dependence of $\overline{X}/D$) as a function of the post-neutron-emission mass and correcting it accordingly. Finally, using the final calculated energies one gets the cos (θ) distribution in the c.m. system:

$$\cos\theta^{\text{c.m.}} = \sqrt{1 - \frac{E_{\text{pre}}^{\text{lab}}}{E_{\text{pre}}^{\text{c.m.}}}(1 - \cos^2\theta^{\text{lab}})}. \qquad (9)$$

The angular anisotropy is calculated relative to the isotropic cos (θ) distribution of $^{235}\text{U}(n_{\text{th}}, f)$. A ratio between the cos (θ) distributions of ^{234}U and ^{235}U is fitted with Legendre polynomials up to the fourth order:

$$\begin{aligned} W_4(\theta) = {} & A_0 + A_0A_2(1.5\cos^2\theta - 0.5) \\ & + A_0A_4(4.375\cos^4\theta - 3.75\cos^2\theta + 0.375). \end{aligned} \qquad (10)$$

The fitted range was $0.3 \leqslant \cos(\theta) \leqslant 0.9$; cos ($\theta$) values outside this range were excluded due to the degraded angular resolution. The respective Legendre polynomial distributions are plotted in Fig. 3(a) as a function of emission angle θ. A

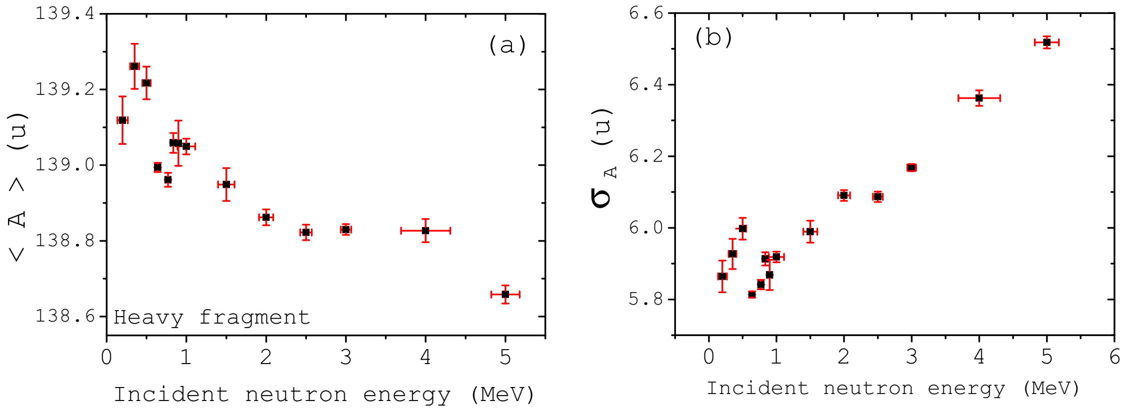

FIG. 5. (a) The average heavy fragment pre-neutron mass decreases as a function of incident neutron energy. (b) The width of the mass distribution increases as a function of neutron energy. Uncertainties in the x direction show the incident-neutron-energy spread (see Table I); uncertainties in the y direction are statistical only.

strong anisotropy at $E_n = 0.835$ and 0.5 MeV can be seen in the vicinity of the vibrational resonances. Note that the maximum at $E_n = 0.835$ MeV is slightly shifted from the resonance peak at $E_n = 0.77$ MeV. A common quantification of the amount of angular anisotropy is given by the ratio $W(0^\circ)/W(90^\circ)$ which is calculated by

$$\frac{W(0^o)}{W(90^o)} = \frac{1 + A_2 + A_4}{1 - 0.5A_2 + 0.375A_4}. \tag{11}$$

Figure 3(b) shows the anisotropy as a function of the incident-neutron energy. The strong angular anisotropy of ^{234}U(n,f) has been the subject of multiple studies [1–3]. The angular distributions measured in this work agree well and verify these earlier findings. Legendre polynomials up to the second degree, P_2, were also tested to fit the data. The P_4 degrees fit the data better; however, the differences are small compared to P_2. See Ref. [12] for details.

B. Mass and energy distributions

As mentioned earlier, no measured yield distributions are available for ^{234}U(n,f). Fourteen mass distributions were measured in this work at the incident-neutron energies listed in Table I. All pre-neutron-emission mass distributions are plotted in Fig. 4. In addition to the absolute yields we plotted the difference in absolute mass for each E_n compared to a chosen reference at $E_n = 2.0$ MeV. The yield difference was calculated as $\Delta Y = Y(2\text{ MeV}) - Y(E_n)$. The mass distribution is more asymmetric at lower neutron energies. Since the liquid-drop contribution increases as a function of fragment mass, the fraction of the symmetric fission component becomes larger. The variations in average heavy mass are shown in Fig. 5(a) as a function of E_n. As indicated earlier, the $\langle A_H \rangle$ decreases, which is partly due to higher symmetric fission yield. Figure 5(b) shows the width of the mass-peak distribution, which increases with neutron energy. This trend observed at higher excitation energies is similar to the cases of ^{238}U(n,f) [8] and ^{237}Np(n,f) [24] and is in agreement with expectations when the liquid-drop contribution increases. In the vicinity of the 0.77-MeV resonance, some more structure is observed in the $\langle A_H \rangle$ and in σ_A.

The $\overline{\text{TKE}}$ distribution as a function of fragment mass is plotted for three cases in Fig. 6(a). The maxima of the mean TKE are found around mass 105 and 130 u. The $\overline{\text{TKE}}$ is also found to decrease as a function of excitation energy. As seen for $E_n = 5.0$ MeV, it mainly drops for $\langle A_H \rangle \lesssim 130$. A similar trend was reported for ^{235}U(n,f) [25] and ^{237}Np(n,f) [24]. The width of the TKE distribution is also plotted as a function of neutron energy in Fig. 6(b). A slight width increase can be inferred from the data as a function of E_n. The $\overline{\text{TKE}}$ difference as a function of fragment mass is shown in Fig. 7 for four cases. The difference is again calculated relative to a reference at $E_n = 2.0$ MeV as $\Delta\overline{\text{TKE}} = \overline{\text{TKE}}(2\text{ MeV}) - \overline{\text{TKE}}(E_n)$.

C. Average changes in mass and TKE distributions

The changes in $\overline{\text{TKE}}$ are listed in Table II and plotted in Fig. 8. The following observations were made:

(1) An increasing $\overline{\text{TKE}}$ occurred at the main vibrational resonance, $E_n = 0.77$ MeV, reaching about 0.4 MeV higher than at $E_n = 1.0$–2.0 MeV. A larger $\overline{\text{TKE}}$ was also reported in ^{238}U in correlation to vibrational resonances [9].

(2) The $\overline{\text{TKE}}$ values for higher incident-neutron energies, $E_n = 3.0$–5.0 MeV, show a decrease similarly to the findings for ^{235}U(n,f) reported in Ref. [6]. As observed earlier in Fig. 6(a), it is for $\langle A_H \rangle \lesssim 135$ u where the $\overline{\text{TKE}}$ decreases.

The kinetic energy release in ^{234}U(n,f) was reported once before, in Ref. [4]. Instead of a higher $\overline{\text{TKE}}$, a lower one was reported at the vibrational resonance as seen in Fig. 8. We believe this discrepancy can be explained by the different solid angle coverage between the two measurements. The use of surface-barrier detectors reduced the solid angle coverage compared to the TFGIC which was used in this work. Our findings show a higher $\overline{\text{TKE}}$ at the resonance, coming mainly from fragments emitted at larger angles. Support for this idea can be found in Ref. [4] since the average fragment kinetic

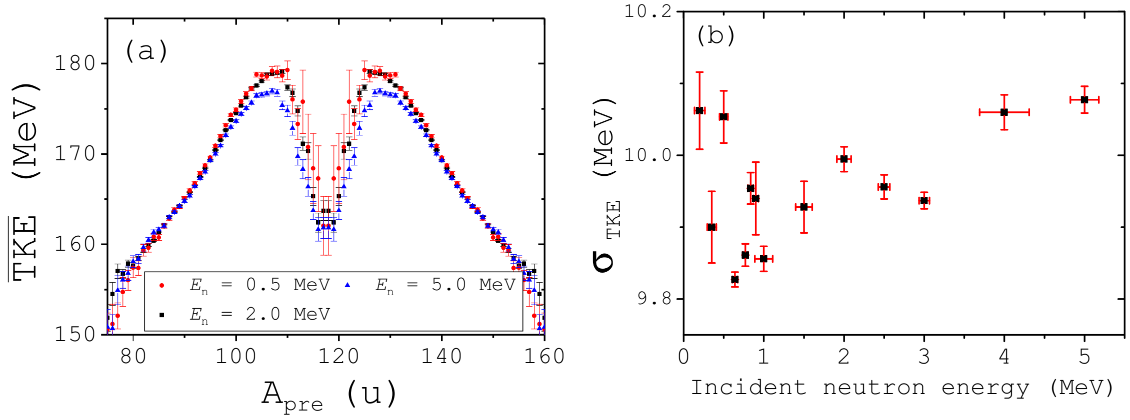

FIG. 6. (a) The $\overline{\mathrm{TKE}}$ distribution as a function of fragment mass for three cases at $E_n = 0.5$, 2.0, and 5.0 MeV. (b) The σ_{TKE} as a function of incident neutron energy. Uncertainties in the x direction show the incident-neutron-energy spread (see Table I); uncertainties in the y direction are statistical only.

energy was actually found to be dependent on the emission angle. Larger average fragment energies were reported for emission angles at 90° compared to 0°.

In this work we studied further the fragment $\overline{\mathrm{TKE}}$ and $\langle A_H \rangle$ as a function of cos (θ). It was found that both these FF observables are dependent on the emission angle. The results show a correlation between the angular dependencies and the vibrational resonances at $E_n = 0.5$ and 0.77 MeV [12,26]. We believe that the vibrational resonances introduce a small but noticeable angular dependency in the mass distribution with a slightly increased $\langle A_H \rangle$ value for the preferred fragment emission direction. This behavior is more-or-less observed at both resonances. The $\overline{\mathrm{TKE}}$ was more than 1 MeV higher at 90° compared to 0° at $E_n = 0.77$ MeV, which was also reported in Ref. [4]. The opposite trend seems to be present for the resonance at $E_n = 0.5$ MeV. The inverted angular anisotropy introduces a lower $\overline{\mathrm{TKE}}$ for 90°. These changes were found to correlate to interesting changes in the mass distribution. These results are the subject of a forthcoming publication [12,26].

It should be noted here that these effects would be removed if we chose to correct for the energy losses individually as described in Sec. III C. If the wrong energy-loss correction method is applied, the angular dependency is removed since it is corrected as a part of the energy losses. However, since the

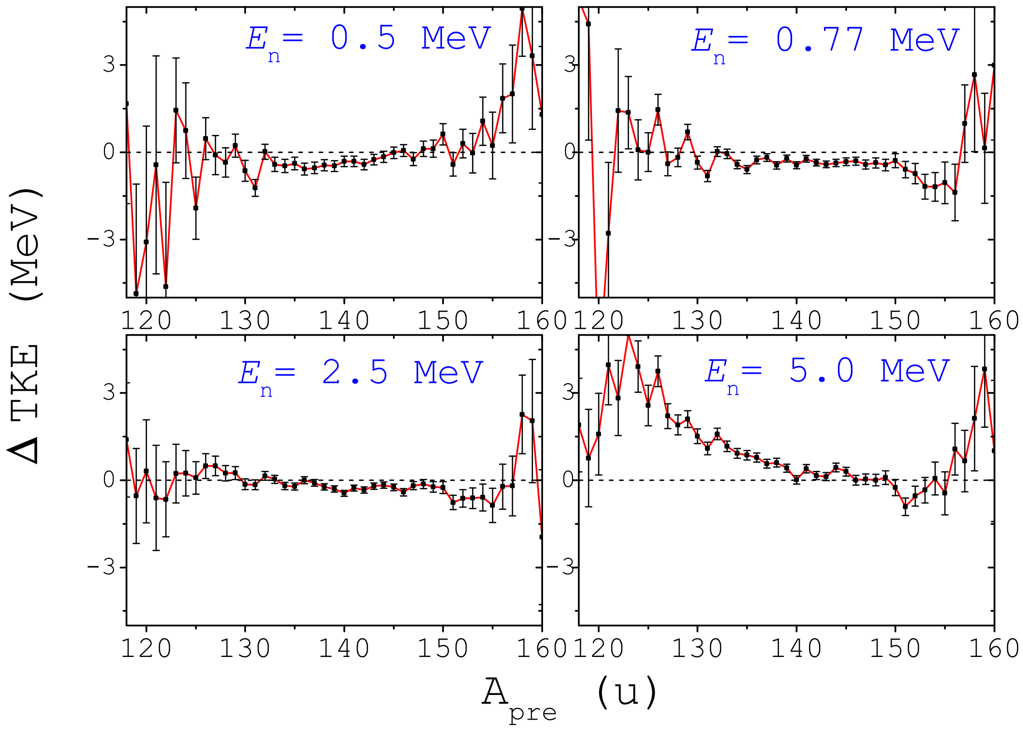

FIG. 7. The $\overline{\mathrm{TKE}}$ difference as a function of fragment mass. The difference is calculated relative to $E_n = 2.0$ MeV as $\Delta\overline{\mathrm{TKE}} = \overline{\mathrm{TKE}}(2\ \mathrm{MeV}) - \overline{\mathrm{TKE}}(E_n)$.

TABLE II. The data on angular anisotropy, $\overline{\mathrm{TKE}}$, and $\langle A_\mathrm{H}\rangle$ for the measurements.

E_n (MeV)	$W(0^\circ)/W(90^\circ)$	$\overline{\mathrm{TKE}}$ (MeV)	σ_TKE (TKE)	$\langle A_\mathrm{H}\rangle$ (u)	σ_A (u)
0.200 ± 0.066	1.107 ± 0.061	170.72 ± 0.08	10.06 ± 0.05	139.12 ± 0.06	5.86 ± 0.04
0.350 ± 0.057	0.766 ± 0.053	170.18 ± 0.07	9.90 ± 0.05	139.26 ± 0.06	5.93 ± 0.04
0.500 ± 0.052	0.644 ± 0.038	170.58 ± 0.05	10.05 ± 0.04	139.22 ± 0.04	6.00 ± 0.03
0.640 ± 0.035	1.036 ± 0.017	170.69 ± 0.02	9.83 ± 0.01	139.00 ± 0.01	5.81 ± 0.01
0.770 ± 0.033	1.600 ± 0.024	170.80 ± 0.02	9.86 ± 0.02	138.96 ± 0.02	5.84 ± 0.01
0.835 ± 0.034	1.767 ± 0.033	170.94 ± 0.03	9.95 ± 0.02	139.06 ± 0.03	5.91 ± 0.02
0.900 ± 0.032	1.575 ± 0.066	170.91 ± 0.07	9.94 ± 0.05	139.06 ± 0.06	5.87 ± 0.04
1.000 ± 0.111	1.202 ± 0.021	170.53 ± 0.03	9.86 ± 0.02	139.05 ± 0.02	5.92 ± 0.02
1.500 ± 0.103	1.211 ± 0.047	170.53 ± 0.05	9.93 ± 0.04	138.95 ± 0.04	5.99 ± 0.03
2.000 ± 0.089	1.227 ± 0.025	170.54 ± 0.02	10.00 ± 0.02	138.86 ± 0.02	6.09 ± 0.02
2.500 ± 0.072	1.222 ± 0.023	170.74 ± 0.02	9.96 ± 0.02	138.82 ± 0.02	6.09 ± 0.02
3.000 ± 0.065	1.199 ± 0.014	170.18 ± 0.02	9.94 ± 0.01	138.83 ± 0.02	6.17 ± 0.01
4.000 ± 0.309	1.105 ± 0.033	170.04 ± 0.04	10.06 ± 0.02	138.83 ± 0.03	6.36 ± 0.02
5.000 ± 0.177	1.115 ± 0.022	169.91 ± 0.03	10.08 ± 0.02	138.66 ± 0.02	6.52 ± 0.02

same ^{234}UF$_4$ sample was used in all measurements, the proper energy-loss correction is to keep the correction curve constant, plotted in Fig. 2(a), instead of determining an individual energy-loss curve for each measured energy.

As discussed in Sec. III E, a second analysis method was performed independently to address different trends in the increasing neutron emission as a function of excitation energy [23,27]. The impact on the observed mass and energy distributions was studied on the two highest neutron energies and was found to be significant, where a relative difference of 20–30% was faced in some isotopes in the post-neutron-emission mass distribution. The average values were also affected where the average mass peak (post) was shifted by 0.68 amu and the $\overline{\mathrm{TKE}}$ changed by roughly 0.2 MeV. Different experimental efforts are ongoing to search for the correct trend in the neutron multiplicity increment [28].

D. Fission-mode parametrization

The experimental data presented in this work were fitted within a fission-mode representation based on Eq. (12) [29].

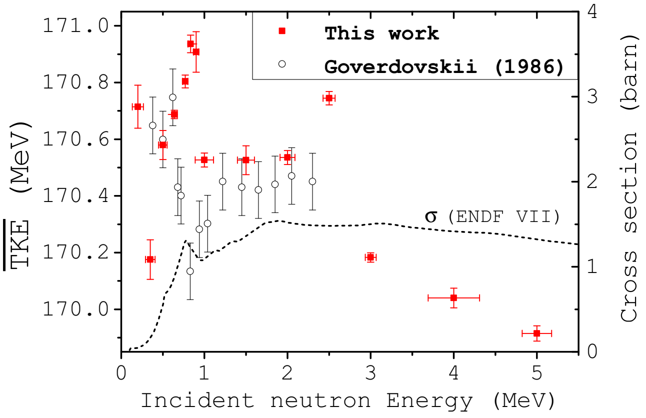

FIG. 8. Changes in the $\overline{\mathrm{TKE}}$ as a function of incident-neutron energy. The data of Ref. [4] (circles) were renormalized to the new known ^{235}U(n_th, f) standard (from 172.25 to 170.5 MeV).

Fission-mode models [29,30] link the early fission-mode interpretation [31] with the potential-energy landscape. The different modes correspond to individual paths in the energy landscape which lead to fission and each mode is characterized with a pre-scission shape which gives a characteristic mass and TKE distribution. Three fission modes at least are needed to fit the two-dimensional mass versus TKE distribution. The symmetric distribution part is fitted with one fission mode denoted superlong (SL). The asymmetric part in the mass distribution is fitted with two modes, the standard-1 (S1) and standard-2 (S2). S1 corresponds to a lower degree of asymmetry and a higher average TKE. Each fission mode is described by a combination of Gaussian functions:

$$Y_m(A,\mathrm{TKE}) = \frac{w_m}{\sqrt{2\pi\sigma_A^2}}\exp\left(-\frac{(A-\langle A\rangle)^2}{2\sigma_A^2}\right)\left(\frac{200}{\mathrm{TKE}}\right)^2 \times\exp\left(\frac{2(d_\mathrm{max}-d_\mathrm{min})}{d_\mathrm{dec}}-\frac{L}{d_\mathrm{dec}}-\frac{(d_\mathrm{max}-d_\mathrm{min})^2}{L d_\mathrm{dec}}\right). \quad (12)$$

The first part of Eq. (12) represents a Gaussian distribution for the mass peak at the mean mass $\langle A\rangle$. The Gaussian height is related by w_m and σ_A is the width of the Gaussian distribution. The second part of Eq. (12) represents a skewed Gaussian distribution to the TKE data (skewed in order to respect the Q-value limit). The parameter d_max gives the distance at highest fission yield probability (around the mass distribution peaks) and d_min is the minimum distance between the fragment charge centers. The parameter d_dec describes the exponential decrease of the yield when d is increasing. The term L is given by

$$L = d - d_\mathrm{min} = \frac{Z_\mathrm{L} Z_\mathrm{H} e^2}{\mathrm{TKE}} - d_\mathrm{min} \approx \frac{A_\mathrm{L} A_\mathrm{H} (Z_\mathrm{CN}/A_\mathrm{CN})^2 e^2}{\mathrm{TKE}} - d_\mathrm{min}, \quad (13)$$

where Z_CN, Z_L, and Z_H are the charges of the compound nucleus and light and heavy fragments, respectively. The parameter d relates to the distance between the centers of the two fission fragments. The approximated distance between the fragment centers d is given by the pure Coulomb interaction. The approximation in Eq. (13) is justified because the charges Z_L and Z_H are not measured in this experiment so one has to assume an unchanged charge distribution, i.e., that $Z_L/A_L \approx Z_H/A_H \approx Z_{CN}/A_{CN}$. It is important to fit both mass and the TKE distribution simultaneously [32]. Six parameters are needed to fit one fission mode to the two-dimensional distribution. To get a good fit to the data some parameters had to be kept fixed. As encountered in earlier works [9,33], $d_{\min}$ had to be fixed to 11.8 fm in order to avoid nonphysical convergence. This was done for all three modes. In the case of the symmetric SL mode, due to the low yield at symmetric fission, the fit procedure was performed for a reference energy and all parameters were kept fixed for the other measurements except for the height parameter (w). An example of the fitted $Y(A,\mathrm{TKE})$ distribution based on Eq. (12) and including three modes is shown in Fig. 9, where the modes are superimposed.

The projection on the mass axis is shown in Fig. 10(a) for $E_n = 2.0$ MeV. Typically a yield ratio of S1/S2 = 1/4 is formed. Figure 10(b) shows the $\overline{\mathrm{TKE}}$ for each mode. As stressed earlier, the highest TKE is attributed to the S1 mode due to the compact pre-scission shape which gives the shortest distance between the fragment centers. The S2 mode is more elongated and shows lower TKE, whereas the SL mode has the longest neck and thus is the lowest energetically.

The results from the mode fits indicate that the relative S1 mode weight increases slightly or stays constant as a function of incident-neutron energy and is not decreasing as in the cases of ^{238}U(n,f) [8] and ^{237}Np(n,f) [24]. This seems to be in agreement with the expectations reported in Ref. [32] as ^{234}U(n,f) should be an "increaser." At the main vibrational resonance, a local increase, by a few percent, is seen. The $\langle A_H \rangle$ of S2 scatters with no apparent dependence on incident-neutron energy. Therefore, to focus on the changes in mode weight, by reducing the degrees of freedom, the $\langle A_H \rangle$ of S2 was kept constant at 140.2 u. After fixing the S2 mass parameter, the increase of the S1 yield was more clear at the vibrational resonance as seen in Fig. 11(a). The increase of the S1 yield is consistent with the earlier findings on the $\overline{\mathrm{TKE}}$. A higher S1 gives higher $\overline{\mathrm{TKE}}$ values and at $E_n = 0.77$ MeV we found both a higher $\overline{\mathrm{TKE}}$ and a higher S1 yield. Note that the SL mode is very small at these low excitation energies and hence the yield of S2 is given by 100% Y(S1). The fission-mode data are listed in Table III. The mode weight uncertainties were estimated by taking into account the correlation matrix from the fit.

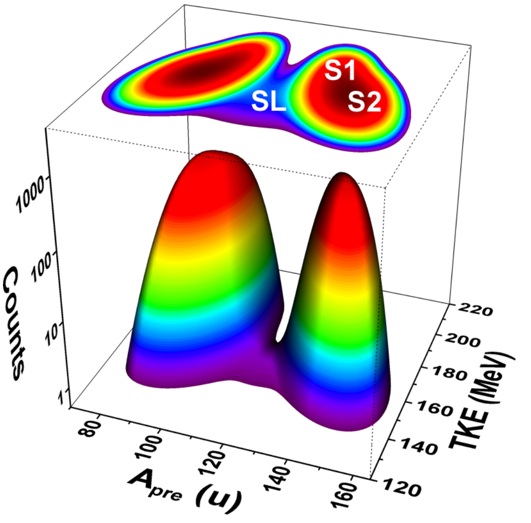

FIG. 9. The experimental two-dimensional TKE vs mass data is fitted with three modes. Equation (12) was used to parametrize the data. In total, three fission modes (S1, S2, and SL) were taken into account.

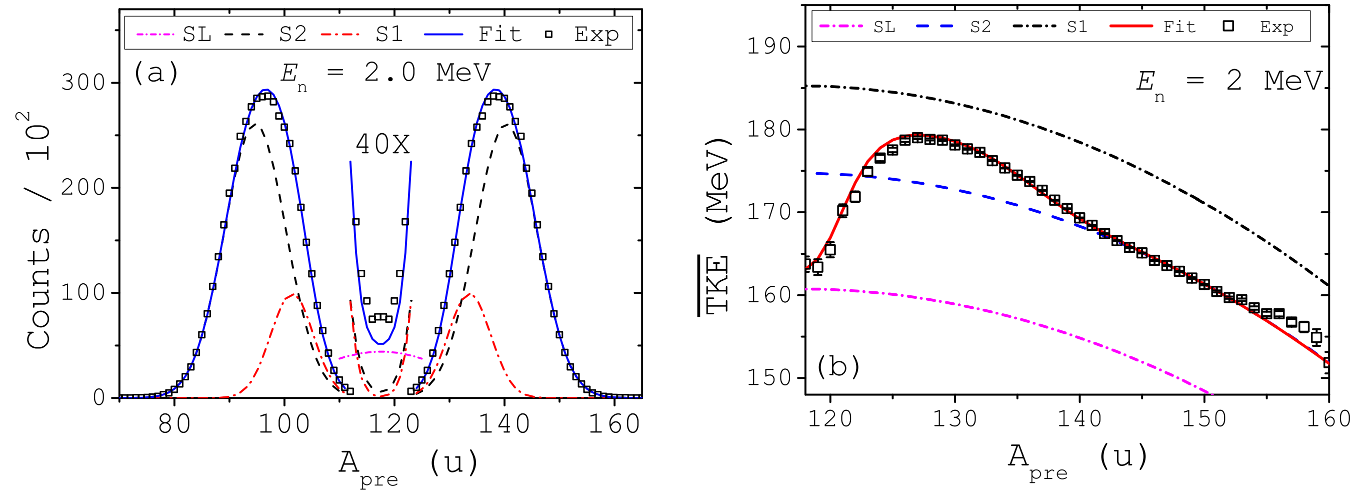

FIG. 10. (a) The experimental $Y(A)$ distribution (points) compared to the mode fit (lines). The S1/S2 yield ratio is usually 1/4. The symmetric distribution part was enlarged by a factor of 40. (b) The experimental $\overline{\mathrm{TKE}}$ as a function of mass compared to the mode fit (lines). The S1 mode yields the highest $\overline{\mathrm{TKE}}$.

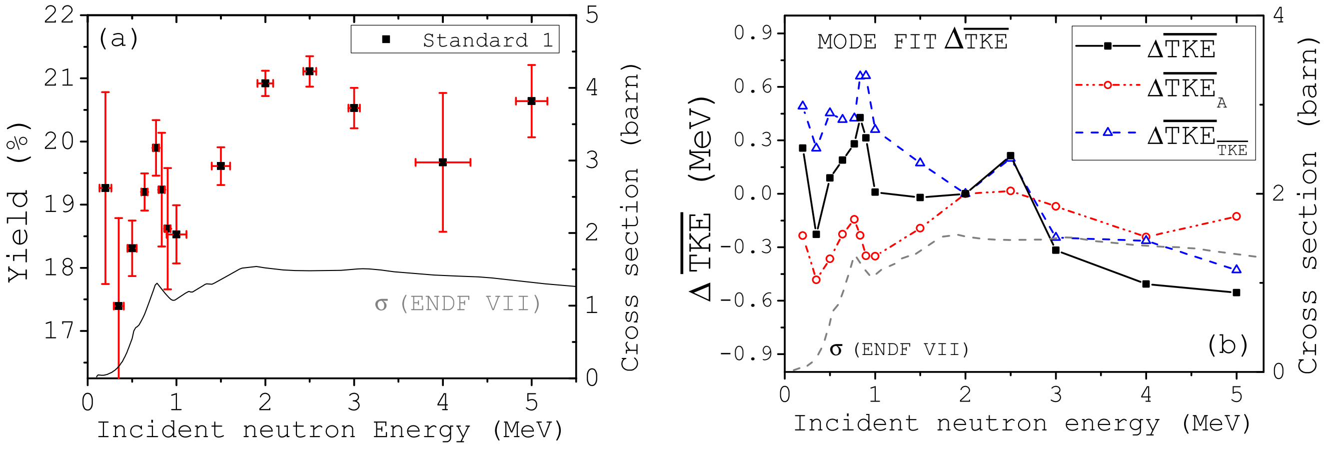

FIG. 11. (a) The relative weight of the S1 fission mode. The errors are calculated based on the correlation matrix. (b) Individual contributions of fission mode TKE and mass, to the total change in $\overline{\mathrm{TKE}}$ as calculated from Eq. (14).

E. Individual contribution from mass and TKE

We also investigated the trends observed in the $\overline{\mathrm{TKE}}$ of Fig. 8(a). The differences in $\overline{\mathrm{TKE}}$ as a function of excitation energy can result from changes in the relative mode weight. However, changes in $\overline{\mathrm{TKE}}_m$ are also due to changes of the intrinsic $\overline{\mathrm{TKE}}$ for each fission mode (m) [7]. Both calculations are made relative to the reference energy $E_\mathrm{n} = 2.0$ MeV. The change of $\overline{\mathrm{TKE}}$ can be written as the sum of both contributions from yield and $\overline{\mathrm{TKE}}$ changes, respectively:

$$\Delta\overline{\mathrm{TKE}} = \Delta\overline{\mathrm{TKE}}_\mathrm{A} + \Delta\overline{\mathrm{TKE}}_\mathrm{TKE}, \tag{14}$$

where both terms are given by

$$\Delta\overline{\mathrm{TKE}}_\mathrm{A} = \frac{1}{2}\sum_{m=1}^{3}(Y(m)_{2.0} - Y(m)_{E_\mathrm{n}}) \times \left(\frac{\overline{\mathrm{TKE}}(m)_{2.0} + \overline{\mathrm{TKE}}(m)_{E_\mathrm{n}}}{2}\right) \tag{15}$$

and

$$\Delta\overline{\mathrm{TKE}}_\mathrm{TKE} = \frac{1}{2}\sum_{m=1}^{3}(\overline{\mathrm{TKE}}(m)_{2.0} - \overline{\mathrm{TKE}}(m)_{E_\mathrm{n}}) \times \left(\frac{Y(m)_{2.0} + Y(m)_{E_\mathrm{n}}}{2}\right). \tag{16}$$

The summation takes into account the three fission modes (m). The calculated trends of $\Delta\overline{\mathrm{TKE}}_\mathrm{A}$ and $\Delta\overline{\mathrm{TKE}}_\mathrm{TKE}$ are shown in Fig. 11(b). The $\Delta\overline{\mathrm{TKE}}$ mostly follows the trend of $\Delta\overline{\mathrm{TKE}}_\mathrm{TKE}$; however, a clear change in $\Delta\overline{\mathrm{TKE}}_\mathrm{A}$ is observed at the resonance, which contributes to the increasing total $\overline{\mathrm{TKE}}$. Such trends were also reported in the cases of $^{235,238}\mathrm{U}(n,f)$ [6,8] and $^{237}\mathrm{Np}(n,f)$ [24].

V. CONCLUSIONS

In this work we investigated the neutron-induced fission of $^{234}\mathrm{U}$ for which experimental data have so far been rather scarce. In particular, no mass yield distributions were available in the data libraries. This study covered the neutron

TABLE III. Data from the fission-mode fits for all measurements after setting A_H of S2 to 140.2 u. See text for details.

E_n (MeV)	S1 Yield (%)	S1 $\langle A_\mathrm{H}\rangle$ (u)	S1 $\overline{\mathrm{TKE}}$ (MeV)	S2 Yield (%)	S2 $\overline{\mathrm{TKE}}$ (MeV)
0.200 ± 0.066	19.26 ± 1.53	134.21 ± 0.17	182.55 ± 0.16	80.34 ± 2.72	168.08 ± 0.10
0.350 ± 0.057	17.39 ± 1.39	134.03 ± 0.15	182.62 ± 0.16	82.46 ± 2.44	167.78 ± 0.09
0.500 ± 0.052	18.31 ± 0.44	134.06 ± 0.05	182.94 ± 0.05	81.44 ± 0.64	167.94 ± 0.03
0.640 ± 0.035	19.20 ± 0.30	133.83 ± 0.03	181.95 ± 0.04	80.52 ± 0.38	168.14 ± 0.02
0.770 ± 0.033	19.90 ± 0.44	133.77 ± 0.04	181.80 ± 0.05	79.67 ± 0.56	168.19 ± 0.03
0.835 ± 0.034	19.24 ± 0.91	133.96 ± 0.06	182.69 ± 0.07	80.42 ± 0.78	168.26 ± 0.04
0.900 ± 0.033	18.62 ± 0.96	133.91 ± 0.06	182.86 ± 0.07	80.76 ± 0.84	168.22 ± 0.05
1.000 ± 0.111	18.53 ± 0.46	133.78 ± 0.05	182.11 ± 0.06	80.89 ± 0.62	168.03 ± 0.03
1.500 ± 0.103	19.61 ± 0.30	133.68 ± 0.03	182.03 ± 0.03	79.90 ± 0.38	167.81 ± 0.02
2.000 ± 0.089	20.92 ± 0.21	133.55 ± 0.02	181.49 ± 0.02	78.69 ± 0.26	167.73 ± 0.01
2.500 ± 0.072	21.11 ± 0.24	133.62 ± 0.02	181.41 ± 0.03	78.39 ± 0.30	168.00 ± 0.02
3.000 ± 0.065	20.53 ± 0.32	133.51 ± 0.03	180.94 ± 0.04	78.89 ± 0.38	167.56 ± 0.02
4.000 ± 0.309	19.67 ± 1.11	133.78 ± 0.07	181.05 ± 0.08	79.14 ± 0.91	167.51 ± 0.05
5.000 ± 0.177	20.64 ± 0.57	133.48 ± 0.06	180.13 ± 0.06	77.98 ± 0.72	167.54 ± 0.04

energy range $E_n = 0.2$–5.0 MeV and we measured angular, energy, and mass distributions at 14 different incident-neutron energies. The main results are summarized as follows:

Angular anisotropy. The ^{234}U(n,f) reaction shows a strong angular anisotropy in the sub-barrier region which peaks at $E_n = 0.835$ MeV and dips at $E_n = 0.5$ MeV. Legendre polynomials (up to fourth order) were used to fit the experimental data. Earlier studies of the ratio $W(0^\circ)/W(90^\circ)$ could be verified [1–3] as seen in Fig. 3.

$\overline{\mathrm{TKE}}$. We found an increasing $\overline{\mathrm{TKE}}$ for ^{234}U(n,f) at incident-neutron energies coinciding with the vibrational resonance as shown in Fig. 8(a). The only earlier measurement from Ref. [4] showed a lower $\overline{\mathrm{TKE}}$. A possible explanation in terms of differences in the solid angle coverage is given in this work, since the $\overline{\mathrm{TKE}}$ for $E_n = 0.77$ MeV was found to be higher for larger angles in contrast to angles near 0°. For higher E_n the $\overline{\mathrm{TKE}}$ is decreasing, similar to observations for ^{235}U(n,f) [6].

Mass and TKE anisotropy. The angular anisotropy at the vibrational resonance is correlated with changes in the mass and TKE distributions. The mass distribution shows a higher $\langle A_H \rangle$ at 0° than at 90° (with implication on the $\overline{\mathrm{TKE}}$). At $E_n = 0.5$ MeV, where the angular anisotropy has opposite sign, the opposite behavior of the mean fragment characteristics is observed. Details will be discussed in a forthcoming publication [12,26].

Fission modes. The fission mode parametrization shows that the standard-1 fission mode yield is increasing as a function of excitation energy and locally at the main vibrational resonance, $E_n = 0.77$ MeV. The parametrization also shows that changes in both the mass and TKE distributions contribute to the observed higher $\overline{\mathrm{TKE}}$ at the main resonance. The anisotropy in mass emission could be understood by modern fission models [29,30]. The S1 and S2 modes are predicted to have slightly different outer barrier heights and could theoretically have different angular distributions (see Ref. [5], p. 494).

ACKNOWLEDGMENTS

The authors would like to thank the staff of the Van de Graaff accelerator at the JRC-IRMM, Geel, Belgium, for providing a stable neutron beam. A.A. acknowledges the European Commission for the fellowship support.

---

[1] J. E. Simmons and R. L. Henkel, Phys. Rev. **120**, 198 (1960).
[2] R. Lamphere, Nucl. Phys. **38**, 561 (1962).
[3] A. N. Behkami, J. H. Roberts, W. Loveland, and J. R. Huizenga, Phys. Rev. **171**, 1267 (1968).
[4] A. A. Goverdovskii, B. D. Kuzminov, V. F. Mitrofanov, and A. I. Sergachev, Sov. J. Nucl. Phys. **44**, 179 (1986).
[5] *The Nuclear Fission Process*, edited by C. Wagemans (CRC Press, Boca Raton, FL, 1991).
[6] C. Straede, C. Budtz-Jørgensen, and H.-H. Knitter, Nucl. Phys. A **462**, 85 (1987).
[7] F.-J. Hambsch, H. H. Knitter, C. Budtz-Jørgensen, and J. P. Theobald, Nucl. Phys. A **491**, 56 (1989).
[8] F. Vivès, F.-J. Hambsch, H. Bax, and S. Oberstedt, Nucl. Phys. A **662**, 63 (2000).
[9] E. Birgersson, A. Oberstedt, S. Oberstedt, and F.-J. Hambsch, Nucl. Phys. A **817**, 1 (2009).
[10] A. Al-Adili, F.-J. Hambsch, S. Oberstedt, S. Pomp, and S. Zeynalov, Nucl. Instrum. Methods A **624**, 684 (2010).
[11] A. Al-Adili, F.-J. Hambsch, R. Bencardino, S. Pomp, S. Oberstedt, and S. Zeynalov, Nucl. Instrum. Methods A **671**, 103 (2012).
[12] A. Al-Adili, Ph.D. thesis, Uppsala University, 2013, http://urn.kb.se/resolve?urn=urn:nbn:se:uu:diva-185306.
[13] A. Göök, F.-J. Hambsch, A. Oberstedt, and S. Oberstedt, Nucl. Instrum. Methods A **664**, 289 (2012).
[14] A. Al-Adili, F.-J. Hambsch, R. Bencardino, S. Oberstedt, and S. Pomp, Nucl. Instrum. Methods A **673**, 116 (2012).
[15] S. Zeynalov, O. Zeynalova, F.-J. Hambsch, and S. Oberstedt, Bull. Russ. Acad. Sci.: Phys. **73**, 506 (2009).
[16] C. Budtz-Jørgensen, H.-H. Knitter, C. Straede, F.-J. Hambsch, and R. Vogt, Nucl. Instrum. Methods A **258**, 209 (1987).
[17] S. S. Kapoor, D. M. Nadkarni, R. Ramanna, and P. N. R. Rao, Phys. Rev. **137**, B511 (1965).
[18] F.-J. Hambsch, J. van Aarle, and R. Vogt, Nucl. Instrum. Methods A **361**, 257 (1995).
[19] F. Vivès, Ph.D. thesis, Bordeaux University, 1998 (unpublished).
[20] C. Wahl, At. Data Nucl. Data Tables **39**, 1 (1988).
[21] G. Barreau, A. Sicre, F. Caitucoli, M. Asghar, and T. P. Doan, Nucl. Phys. **432**, 411 (1985).
[22] D. Mather, P. Fieldhouse, and A. Moat, J. Nucl. Phys. **66**, 149 (1965).
[23] A. Al-Adili, F.-J. Hambsch, S. Pomp, and S. Oberstedt, Phys. Rev. C **86**, 054601 (2012).
[24] F.-J. Hambsch, F. Vivés, P. Siegler, and S. Oberstedt, Nucl. Phys. A **679**, 3 (2000).
[25] R. Müller, A. A. Naqvi, F. Käppeler, and F. Dickmann, Phys. Rev. C **29**, 885 (1984).
[26] A. Al-Adili, F.-J. Hambsch, S. Pomp, and S. Oberstedt, Phys. Procedia **31**, 158 (2012).
[27] A. Al-Adili, F.-J. Hambsch, S. Pomp, and S. Oberstedt, Nucl. Data Sheets **119**, 342 (2014).
[28] A. Al-Adili, E. Alhassan, C. Gustavsson, P. Helgesson, K. Jansson, A. Koning, M. Lantz, A. Mattera, A. Prokofiev, V. Rakopoulos *et al.*, Phys. Procedia **64**, 145 (2015).
[29] U. Brosa, S. Grossmann, and A. Müller, Phys. Rep. **197**, 167 (1990).
[30] P. Möller, D. G. Madland, A. J. Sierk, and A. Iwamoto, Nature **409**, 785 (2001).
[31] A. Turkevich and J. B. Niday, Phys. Rev. **84**, 52 (1951).
[32] U. Brosa, H.-H. Knitter, T.-S. Fan, J.-M. Hu, and S. L. Bao, Phys. Rev. C **59**, 767 (1999).
[33] A. Göök, M. Chernykh, C. Eckardt, J. Enders, P. von Neumann-Cosel, A. Oberstedt, S. Oberstedt, and A. Richter, Nucl. Phys. A **851**, 1 (2011).